THE JOURNAL OF PHYSICAL CHEMISTRY C

pubs.acs.org/JPCC Article

One-Step Growth of Core−Shell (PtPd)@Pt and (PtPd)@Pd Nanoparticles in the Gas Phase

Diana Nelli, Anjana Krishnadas, Riccardo Ferrando,* and Chloé Minnai*

Cite This: https://dx.doi.org/10.1021/acs.jpcc.0c02621 Read Online

ACCESS | Metrics & More | Article Recommendations | Supporting Information

ABSTRACT: Pt−Pd nanoparticles are grown in the gas phase by a magnetron-sputtering source and characterized by electron microscopy techniques for both Pt-rich and Pd-rich compositions of the metallic vapor. It is shown that this growth procedure can produce different types of core−shell nanoparticles, in one step, with sizes in the range of 4−10 nm, according to the composition of the vapor being rich either in Pt or in Pd. In all cases, the nanoparticles present intermixed cores containing both Pt and Pd and shells made of the majority element, i.e., of (PtPd)@Pt structure for the Pt-rich vapor and (PtPd)@Pd structure for the Pd-rich vapor. Global searches of the optimal chemical ordering show that none of these structures correspond to equilibrium configurations. On the contrary, these core−shell structures are strongly out-of-equilibrium, being the result of kinetic trapping phenomena. This is verified by molecular dynamics growth simulations which are able to reproduce both the different types of chemical ordering and the variety of geometric shapes found in the experiments.

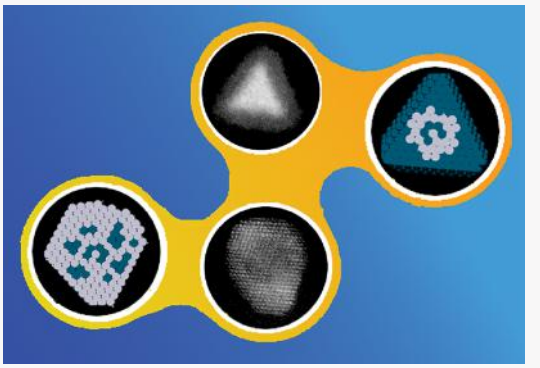

1. INTRODUCTION

Binary metallic clusters and nanoparticles (BNP, also known as *nanoalloys*)[1−5] are receiving increasing attention in recent years due to their versatility in applications. These applications range from catalysis to optics and plasmonics to data storage and biomedicine.

In general, elemental nanoparticles exhibit distinct properties which are different from those of the bulk materials and can be tuned by controlling their size and shape. In addition, BNPs properties are often enhanced with respect to their monometallic counterparts and can be further manipulated by controlling their spatial atomic distribution (i.e., chemical ordering).

In view of their applications, a precise control of size, shape, and chemical ordering of BNPs is highly desirable.[1,6] This requires a deep understanding of the formation mechanisms of BNPs, which can be obtained by combining experiments and computer simulations (see, for example, refs 7−12), which allows a full investigation of the mechanisms at the atomic level.

According to their chemical ordering, BNPs can be classified into core−shell (with either centered or off-center core[13,14]), alloyed, onionlike, and segregated subclusters (Janus and quasi-Janus particles).[4,15] Among these, core−shell structures are particularly attractive as the addiction of a shell offers the possibility of manipulating the NPs through external stimuli,[6,16] controlling the core−distance interaction, and protecting the core from chemical reactions with the environment and impurities.[17,18]

Pt−Pd NPs are the subject of many studies because of their excellent catalytic activity, which has been demonstrated as being superior to that of the corresponding pure elements in several cases.[19−23] Both platinum and palladium are indeed widely used in the chemical industry, for automobile exhaust purification and fuel cells,[24−26] hydrogen oxidation,[27] oxygen reduction,[20,21] and several other electrocatalytic reactions.[19,23,28,29]

Pd(core)@Pt(shell) is often the desired element arrangement of these BNPs as it places the most efficient nanocatalyst (Pt) on the extreme surface of the nanoparticle.[30] However, this arrangement is the less favorable state from an energetic point of view,[31,32] which makes its synthesis particularly complex. In this respect, wet chemical techniques, involving colloidal chemistry in liquid environments, are the most popular approach to synthesize Pt−Pd NPs. So far, random alloy and single-crystalline Pt−Pd NPs,[33] Pt@Pd core−shell structures,[25,34] and a few examples of random alloyed nanocubes, tetragons, and heterostructures[23,28,35] were produced.

Because of its mass production capacities, the chemical synthesis of NPs is widely used but still poses a number of

Received: March 25, 2020
Revised: June 9, 2020
Published: June 10, 2020

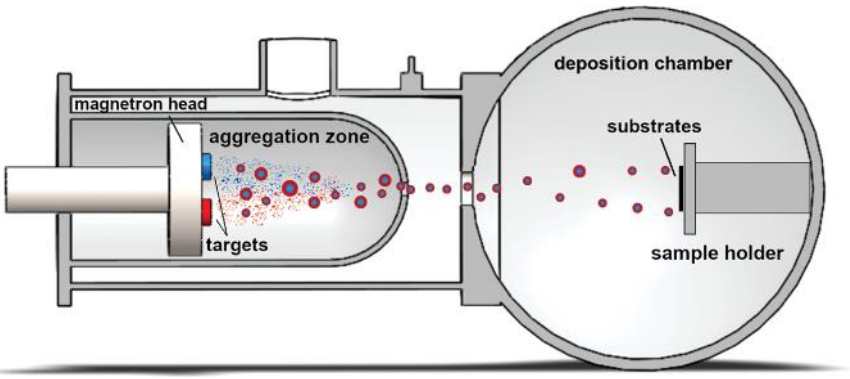

Figure 1. Schematic representation of the deposition system used in this study, including the Nanogen-Trio nanoparticle source from Mantis Deposition, Ltd. Pt and Pd targets are placed on a magnetron head, on the same linear translator. The targets are DC cosputtered in an Ar atmosphere. This generates vapors which condense within a water-cooled aggregation zone. The working pressure in this region is $\sim 10^{-1}$ mbar. The NPs are extracted and accelerated by the differential pressure between the aggregation zone and the deposition chamber which is kept at a pressure of $\sim 10^{-4}$ mbar. The NPs then soft-land on the substrates placed in the deposition chamber (not to scale).

difficulties in obtaining an effective control of size, shape, and element distribution, particularly when strongly out-of-equilibrium structures, such as Pd@Pt NPs, are desired.[17,36] Moreover, for NPs produced in solution, a stabilizing functionalization is necessary to prevent their agglomeration, thus affecting the composition purity and often requiring high-temperature post-treatments which can impact the NPs properties.[37,38]

Alternatively, gas-phase synthesis can be used to produce a wide variety of NPs. A common approach is based on the sputtering of metallic targets followed by a condensation of the atomic vapor into NPs which occurs along the propagation of the vapor through an aggregation zone. With this approach, the chemical ordering, size, and shape of the NPs can be tuned controlling the sputtering parameters.[30,39−42]

Being produced in the gas phase, these NPs are highly pure and surfactant-free, nonagglomerated, and stable.[17] This approach has been widely exploited over the last decades to create NPs with narrow size distributions,[7,43] highly controlled shapes,[11] and specifically designed composite structures.[6,44,45] Besides being the ideal platform for fundamental nanoscience studies, NPs produced in the gas phase constitute also the building blocks for innovative functional materials.[46−56]

At variance with the intense activity to synthesize Pt−Pd NPs by means of wet chemistry processes, very few attempts were made by gas-phase methods. In ref 30 core−shell (PdPt)@Pt NPs with an incomplete Pt shell were obtained by plasma-sputtering deposition in a two-step process. In the first step $Pd_{0.97}Pt_{0.03}$ mixed NPs were formed in the gas phase and landed on a substrate. In the second step, the $Pd_{0.97}Pt_{0.03}$ NPs on the substrate were covered by a Pt shell by further deposition of pure Pt. However, this resulted in a partial covering of the core, only on the exposed side. A few examples of Pt−Pd thin films are also reported in the literature.[27,57]

In the present study we show that a one-step synthesis, which takes place completely in the gas phase without any further deposition after landing on the substrate, allows the production of Pt−Pd NPs with composition-tunable chemical ordering. In these NPs, the minority element always concentrates in the central part of the structure, while the shell is strongly enriched in the majority element. This corresponds to the formation of (PtPd)@Pd and of (PtPd)@Pt core−shell structures in the Pd-rich and Pt-rich cases, respectively. Besides having a controllable and reproducible chemical ordering, these highly pure NPs present a narrow size distribution and soft-land on the substrate creating random arrays of isolated NPs potentially attractive for catalysis-related experiments.

To deeply understand both the physical origin of the observed composition-tunable chemical ordering and the mechanisms leading to the formation of these out-of-equilibrium core−shell structures, we rationalize the experimental results by computer simulations. By means of global optimization searches, we demonstrate that neither (PtPd)@Pd nor (PtPd)@Pt arrangements correspond to the equilibrium chemical ordering but are the result of kinetic trapping phenomena instead. The kinetic origin of these structures is further confirmed by molecular dynamics (MD) simulations of nanoparticle growth, which are able to reproduce both geometric shapes and chemical ordering in very good agreement with the experiments.

2. METHODS AND MODEL

2.1. Experimental Methods. Pt−Pd NPs are synthesized by inert gas-aggregation sputtering deposition (Nanogen-Trio source, Mantis Deposition Ltd., U.K.). This technique is based on the condensation of an atomic vapor produced by DC simultaneous magnetron sputtering of targets.

As schematically shown in Figure 1 and described in detail in refs 44 and 58, the Nanogen-Trio source employs three separate circular 1″ targets mounted on the same linear translator within one region of inert gas aggregation, called the aggregation zone. Each 1″ magnetron has an independent power supply which allows the sputtering current applied to the different targets to be adjusted separately, thereby providing control over the mole fraction of metals incorporated into the NPs.

Here, Pt−Pd NPs are prepared by DC sputtering of separate Pt and Pd targets in an Ar atmosphere of $\sim 10^{-1}$ mbar. The gas ports on the Nanogen-Trio source are designed so that the flow of sputtering gas is directed from the outside of the targets toward their center. This inward direction of gas flow sweeps Ar across the sputtering surfaces and ensures early mixing of the metal vapors generated over the different targets. The saturated vapor of metal atoms condenses into NPs along its propagation path through the aggregation zone.

After the NPs exit the aggregation region, the distribution of NPs (typically fwhm about 2 nm) passes through a 5 mm

https://dx.doi.org/10.1021/acs.jpcc.0c02621
J. Phys. Chem. C XXXX, XXX, XXX−XXX

skimmer and into the MesoQ frequency-scanning quadrupole mass (see refs 59 and 60 and the Supporting Information for details) and reaches a deposition chamber which is at a pressure of 6×10^{-4} mbar. Here, the distribution of NPs softly lands onto substrates held at ground potential. A histogram showing a representative size distribution of Pt−Pd NPs is shown in Figure S1. The kinetic energy of the NPs is estimated to be <1 eV, which is well below the threshold for soft-landing. The amount of soft-landed material is determined by monitoring the ion current during deposition at a wire mesh grid at the exit of the MesoQ.

The number of atoms that can be ejected from the target per sputtering ion (i.e., the sputtering yield) depends on the power applied to the target. Hence, tuning the ratio between the powers applied to the two targets causes the composition of the atomic vapor to be affected, and in turn the chemical composition of the Pt−Pd structures. In particular, to control the chemical ordering of the Pt−Pd NPs, the sputtering currents applied to the targets are adjusted to create either a Pd-rich atomic vapor ($Pd_{0.8}Pt_{0.2}$) or a Pt-rich one ($Pt_{0.7}Pd_{0.3}$). Specifically, the former is obtained by applying powers of 8 and 24 W to the Pt and Pd targets, respectively. The latter is obtained by applying powers of 23 and 8 W to the Pt and Pd targets, respectively.

From those values the chemical composition of the atomic vapor is estimated by dividing the power applied to the target by the cohesion energy of the specific element ($E_{c,Pd}$ = 3.89 eV/atom and $E_{c,Pt}$ = 5.84 eV/atom).

The targets are sputtered in an Ar flux of 60 sccm (standard cubic centimeters per minute), with an aggregation zone length of 125 mm and a pressure of 3×10^{-1} mbar at the Nanogen.

To unravel the element distribution of Pt and Pd in the Pt−Pd NPs as a function of their composition, the NPs are deposited directly on amorphous carbon coated TEM grids to yield random arrays of BNPs. Due to the large difference between the atomic number of Pd (Z = 46) and Pt (Z = 78), a strong contrast between brighter Pt-rich and darker Pd-rich areas is expected in the STEM images, making this technique particularly appropriate to study with high accuracy the element arrangement of Pt−Pd NPs.

The average composition, size, and morphology of the NPs are examined using an aberration-corrected scanning transmission electron microscope (C_s-corrected-STEM), JEOL JEM-ARM 200F (200 kV). The NPs are characterized using high-angle annular dark-field scanning transmission electron microscopy (HAADF-STEM). Scanning transmission electron microscopy combined with X-ray energy-dispersive spectroscopy (STEM−EDX) is also used to study elemental mapping for the respective elements.

Images, spectra, histograms, as well as chemical maps for the elements are obtained using the Digital Micrograph software from Gatan. For each sample about 30 pictures at different magnifications are taken in different region of the sample to have consistent systematic data.

2.2. Model and Simulation Methods. The NPs are modeled by an atomistic force field, derived in the framework of the second-moment approximation to the tight-binding model,[61,62] in which the potential energy E of a cluster is the sum over all the atoms of bonding (E^b) and repulsive (E^r) contributions:

$$E = \sum_j (E_j^b + E_j^r) \tag{1}$$

with

$$E_j^b = -\sqrt{\sum_i \xi_{sw}^2 \exp\left[-2q_{sw}\left(\frac{r_{ij}}{r_{sw}^0} - 1\right)\right]} \tag{2}$$

and

$$E_j^r = \sum_i A_{sw} \exp\left[-p_{sw}\left(\frac{r_{ij}}{r_{sw}^0} - 1\right)\right] \tag{3}$$

r_{ij} is the distance between atoms i and j, s (w) refers to the chemical species of the atom i (j), and r_{sw}^0 is the nearest-neighbor distance in the sw lattice. If the interaction is heteroatomic ($s \neq w$) r_{sw}^0 is expressed as the arithmetic average:

$$r_{PtPd}^0 = \frac{r_{PtPt}^0 + r_{PdPd}^0}{2} \tag{4}$$

The parameters p, q, A, and ξ are taken from ref 31. The interactions are cut off at the second-neighbor distance and linked to zero at the third-neighbor distance by a fifth-order polynomial.

Global optimization searches are made by our Basin Hopping code.[63] Full global searches are made to look for the mixing energy, while the optimization of the chemical ordering at a fixed geometry is made by using exchange moves only. Both random and tailored moves are used.[4] For each system and composition, at least 3 independent simulations of lengths between 5×10^4 and 10^6 steps are made.

MD simulations of the growth are done by depositing atoms one by one on a preformed seed[7,64] with a rate of 1 atom every 10 ns. The equations of motion are solved by the velocity Verlet algorithm with a time step of 5 fs. Temperature is kept constant by an Andersen thermostat, whose collision frequency has been chosen to ensure good thermalization with a negligible perturbation of the dynamics.[65]

3. RESULTS AND DISCUSSION

3.1. Experimental Determination of Chemical Ordering. In light of designing BNPs with a specific chemical composition and chemical ordering, a remarkable advantage of magnetron sputtering deals with the possibility of simultaneously sputtering up to three targets of different materials and, by varying the powers applied to each of the targets, creating multielemental NPs with tunable chemical composition. As we show below, changes in the composition of the vapor crucially impact the resulting chemical ordering of the BNPs. This effect was already observed in the gas-phase growth of Au−Ag NPs of about 2 nm diameter, where it was shown that atoms organize in different chemical arrangements according to their relative abundance in the original vapor, the shell and the core being enriched by the majority and minority elements, respectively.[9] Here below we experimentally show that in Pt−Pd NPs this effect holds for considerably larger sizes, and in Section 3.2 we explain its origin by means of computer simulations.

In the following, we adjust the powers applied to the Pt and Pd targets to obtain either Pt-rich ($Pt_{0.7}Pd_{0.3}$) or Pd-rich ($Pd_{0.8}Pt_{0.2}$) atomic vapors. The different compositions of the atomic vapor will lead to NPs not only with different compositions but also with strikingly different chemical ordering.

https://dx.doi.org/10.1021/acs.jpcc.0c02621
J. Phys. Chem. C XXXX, XXX, XXX−XXX

Let us consider first a sample obtained in the Pt-rich ($Pt_{0.7}Pd_{0.3}$) case and analyze the distribution of NPs at low magnification. The homogeneity of the bimetallic distribution can be checked by performing STEM-EDX analysis, as shown in Figure 2. Separate mappings of Pt and Pd are given in

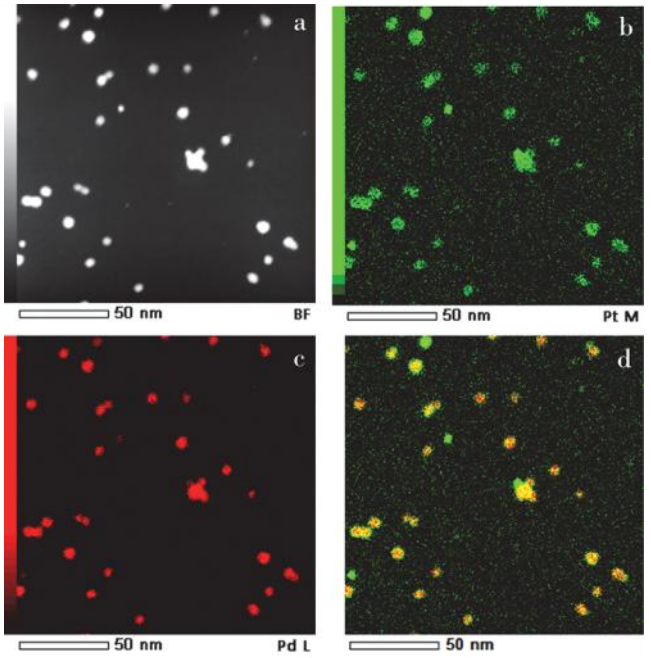

Figure 2. (a) Low-magnification STEM-EDX image of a distribution of Pd−Pt NPs grown in a Pt-rich environment. Separate mappings of Pt and Pd are shown in frame (b) and (c), respectively. Frame (d) shows the composition mapping with Pt and Pd overlaid.

Figures 2b and 2c, respectively, and 2d shows the composition mapping with Pt and Pd overlaid. The Pt and Pd maps reveal the presence of the individual elemental contrasts in the core−shell arrangement of the NPs. At this low magnification, the core−shell structure, with the shell enriched in Pt and the core enriched in Pd, is rather clearly visible only in some NPs (in the half bottom part of the image for instance). However, the true core−shell character of the BNPs will be better demonstrated in the following by analyzing the images at higher magnification. With regard to the size distribution of the NPs of Figure 2, we find that there are two populations, a larger population of average size 5.7 ± 0.8 nm and a smaller population peaked at 1.8 ± 0.4 nm. The average size of the larger population is calculated excluding the five cases of coalescence between NPs.

The smaller population is hardly visible at this magnification; only some NPs can be seen in the top right quarter of the frame. These NPs have fcc crystalline structure and generally are constituted of both Pt and Pd, but without any evidence of core−shell elemental distribution. The presence of sub-2 nm nanoparticles has been reported in pure Ag and Pt samples grown by a magnetron-sputtering source. They were believed to originate from a charging effect of the clusters.[46,66] Similar features were also observed in Pt−Pd systems grown by a chemical synthesis approach.[29] However, in this last case, the sub-2 nm NPs decorated the surface of larger NPs with diameters of ∼20 nm.

Regarding the chemical composition of the particles of Figure 2, we can notice that 4/36 NPs of the frame qualitatively show an almost pure Pt composition, with contamination of small Pd (not visible at this scale). We note that one of these NPs constitutes a lobe of the coalesced structure in the center of the frame, whereas both the central core and the other two lobes present a Pd@Pt structure; on the contrary, pure Pd NPs are not found.

Finally we note that coalescence occurred in 5/36 NPs of this frame and constitutes a phenomenon that we often observe in the distributions.

In this experiment we are interested in analyzing a relatively wide distribution of NPs to gain a broad understanding of the growth of Pt−Pd NPs. We note however that the size distribution could be narrowed down using the mass filter selector as described in Section 2. This would allow to select and deposit one of the above-mentioned populations. In addition, as we observed that particles with similar size exhibit consistent features (in terms, for instance, of chemical ordering, shell thickness, core radius, etc.), this approach would also allow the purification of the NPs distribution as regards chemical ordering.

In Figure 3 we consider the Pd-rich case. Panel 3a shows an HAADF-STEM image at low magnification. The average size

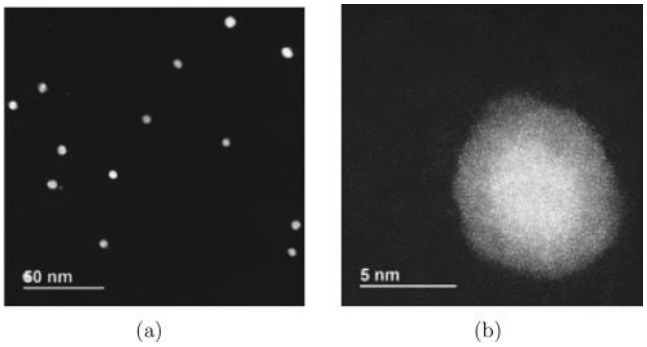

Figure 3. (a) Low-magnification C_s-corrected STEM-HAADF image of a typical distribution of Pt−Pd, showing several NPs. (b) C_s-corrected STEM-HAADF image of a (PtPd)@Pd NP grown in a Pd-rich environment. The scattered intensity scale is associated with the atomic number Z of the elements. This makes it easy to distinguish the heaviest Pt (brighter) from Pd (darker), showing that the Pd-rich zone is in the shell of the NP.

of the NPs is 5.6 ± 0.6 nm; hardly visible at this scale, sub-2 nm NPs can be seen in the left side of the image. At higher magnification, it is possible to see the core−shell structure of the NPs, which we observed in 60−80% of the NPs depending on the sputtering conditions, in both Pd-rich and Pt-rich atmosphere. An example is shown in Figure 3b, where the high Z contrast makes easy to distinguish the bright Pt-rich core from the darker Pd-rich shell. The NP has a diameter of ∼8.4 nm and a core radius of approximately the same length as the shell thickness (i.e., ∼2.4 nm). In this case, the analysis thus hints at the formation of some kind of Pt@Pd core−shell arrangement, i.e., *the opposite of the Pt-rich case*.

In summary, we note that the results shown in Figures 2 and 3b indicate that, in the large NP populations (diameters from 4 nm on), the minority element always concentrates at the NP core, while the shell is enriched in the majority element. On the other hand, smaller NPs (diameters ∼2 nm) containing both elements do not show any clear indication of segregation. These points need to be better discussed by analyzing the NPs at higher magnification with both HAADF-STEM and EDX.

https://dx.doi.org/10.1021/acs.jpcc.0c02621
J. Phys. Chem. C XXXX, XXX, XXX−XXX

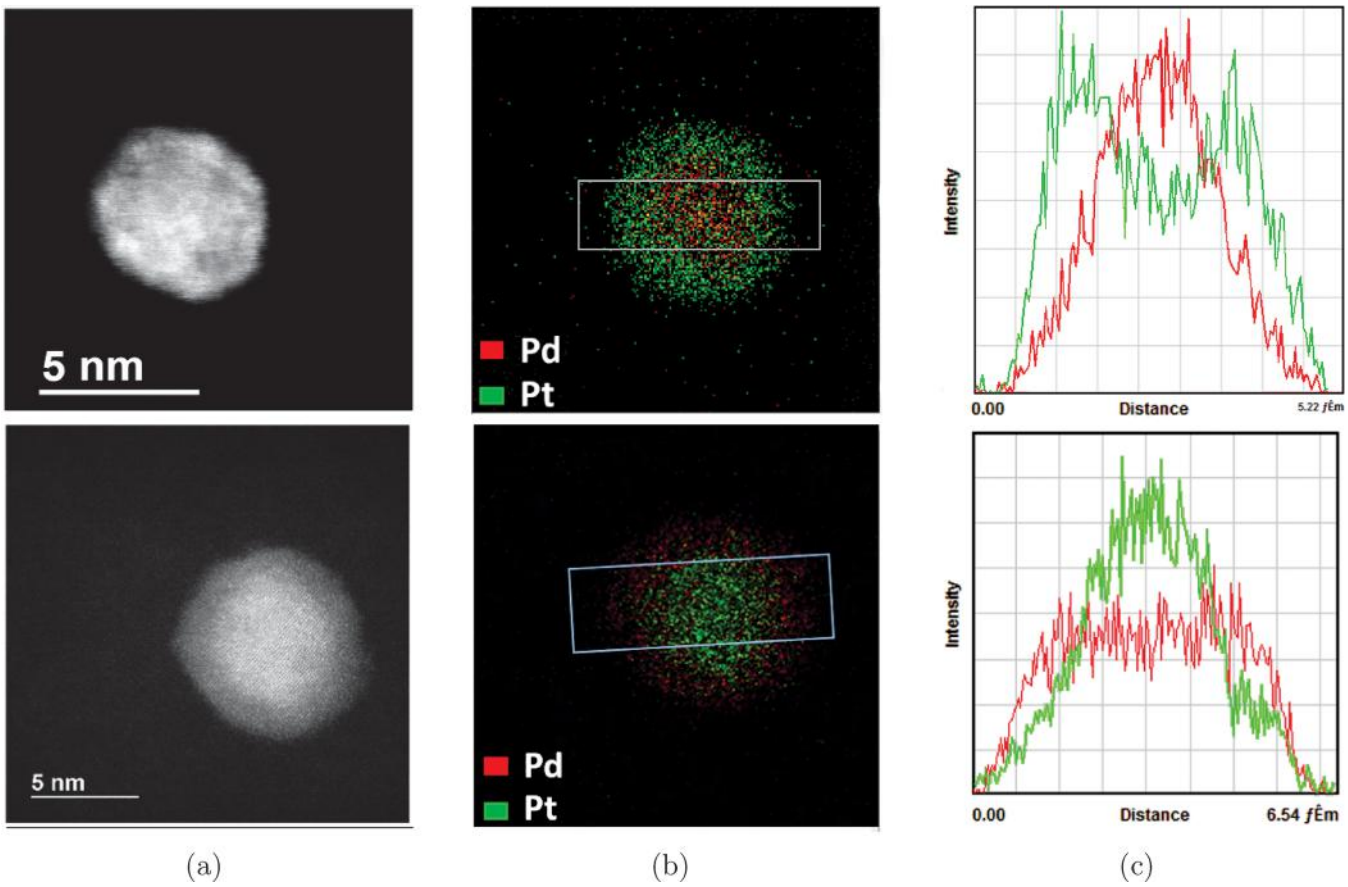

Figure 4. High-magnification image of a (PtPd)@Pt NP (top row) and (PtPd)@Pd NP (bottom row) grown in a Pt-rich and Pd-rich atmosphere, respectively. (a) C_s-corrected HAADF-STEM images of the NPs. The difference in contrast facilitates the distinction between the Pt- and Pd-rich zones of the NPs. (b) STEM−EDX mapping of the chemical composition of the NPs. The colors are based on the chemical composition of the NPs where Pt is in green and Pd in red. The rectangle in the panel indicates the area from which the profiles are extracted. (c) EDX composition profiles Pt in green and Pd in red clearly showing that the Pt-rich zone is in the shell of the NP grown in the Pt-rich atmosphere and in the core of the one grown in the Pd-rich atmosphere.

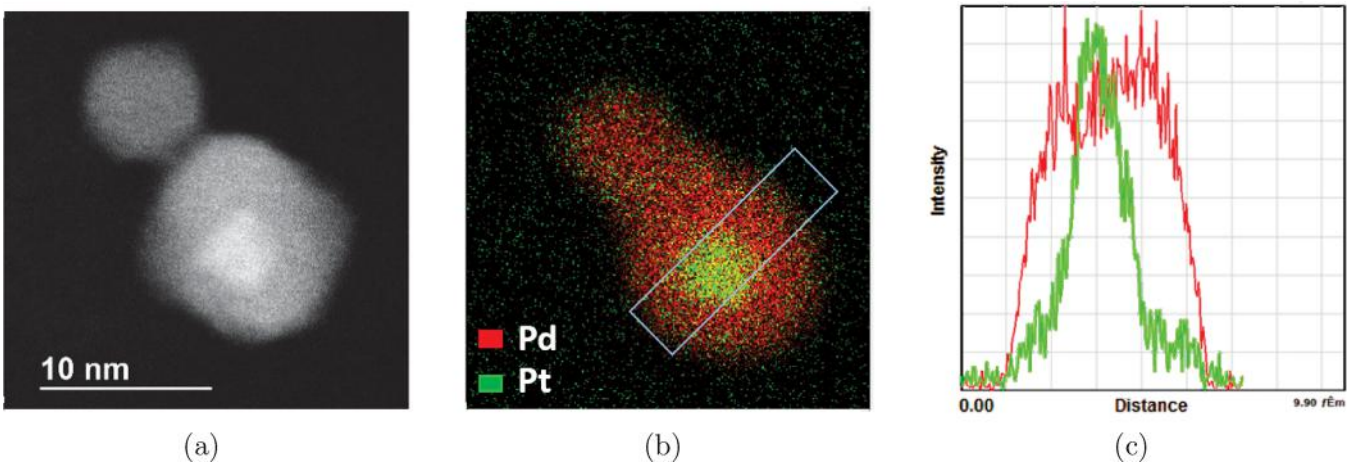

Figure 5. Example of the coalescence of (PtPd)@Pd NPs grown in a Pd-rich atmosphere. From left to right: (a) C_s-corrected HAADF-STEM images of the NPs. (b) STEM−EDX mapping of the chemical composition of the NPs. The rectangle in the panel indicates the area from which the profiles are extracted. (c) EDX composition profiles (Pt in green and Pd in red).

In Figure 4 we present high-magnification images of a Pt-rich NP obtained from a $Pt_{0.7}Pd_{0.3}$ vapor (top row) and of a Pd-rich NP from a $Pd_{0.8}Pt_{0.2}$ vapor (bottom row). In both cases we show (a) the HAADF-STEM image, (b) the EDX chemical maps, and (c) an average of the line scans across the rectangles marked in image (b). The core−shell structure is clearly observed in these images. The core contains both elements in similar proportions, while the shell is strongly enriched in the majority element. In the Pt-rich NP, the Pt constitutes a core ∼5.5 nm large, located roughly in the center

https://dx.doi.org/10.1021/acs.jpcc.0c02621
J. Phys. Chem. C XXXX, XXX, XXX−XXX

of the ∼8.4 nm nanoparticle; the shell mostly contains Pd atoms.

We note also that the core has an fcc crystalline structure while the shell presents both crystalline and amorphous regions. The latter are probably due to the oxidation of Pd. In fact, when Pd is in the core of NPs, it keeps a crystalline structure. On the contrary, Pt shells tend to remain crystalline. These findings are supported by the diffraction analysis of different regions of Pt−Pd NPs, shown in the Supporting Information (Figure S2).

The results of Figure 4 demonstrate that (PtPd)@Pt and (PtPd)@Pd core−shell NPs are grown in Pt-rich and Pd-rich atmospheres, respectively. This result is obtained by a straight control of the powers applied to the two targets, while keeping all other sputtering parameters (argon flow and aggregation zone length) constant. We believe this is remarkably interesting in the case of the (PtPd)@Pt NPs, as this chemical ordering is particularly difficult to be synthesized by wet chemistry approaches, being the less energetically favorable configuration of the two materials.

In summary, by comparing various Pt-rich and Pd-rich NP distributions, we observe mainly four NP types: (i) core−shell NPs with the minority element concentrated in the core and shell made of the majority element; (ii) coalesced NPs; (iii) sub-2 nm NPs; (iv) NPs mainly constituted by the majority element with small contamination of the minority element. In Figures 5−6 we present some more examples to elucidate further features of the NPs.

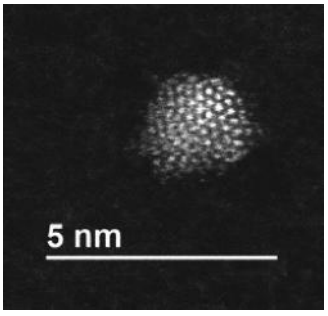

Figure 6. Example of a sub-2 nm NP grown in a Pd-rich atmosphere.

An example of coalescence is presented in Figure 5. Here, the coalescence occurs between a (PtPd)@Pd NP and a smaller particle mainly consisting of Pd with some contamination of Pt. The core−shell particle has a size of ∼10.5 nm and a core of ∼4.5 nm. The smaller particle has a diameter of ∼6.3 nm. Between the two particles we can observe an interface ∼1 nm thick. This is visible in the HAADF-STEM image and not in the EDX mapping since in this case the beam energy forced the complete coalescence between the two structures.

Finally, a sub-2 nm Pt−Pd NP is shown in Figure 6. According to the sputtering conditions, the sub-2 nm population can represent up to the 50% of the whole number of NPs (but this corresponds to a much smaller proportion of material). By performing a chemical analysis, we observe that these particles have a mixed chemical composition with roughly the same amount of the two materials. Interestingly, those NPs do not exhibit a clear core−shell structure, but they look like the mixed cores of the larger core−shell NPs.

3.2. Equilibrium vs Nonequilibrium in Pt−Pd Nanoparticles.

In Section 3.1 we reported the TEM observations of Pt−Pd NPs produced in the gas phase for Pd-rich and Pt-rich compositions of the vapor. In both cases, two populations were obtained: (i) sub-2 nm NPs with intermixed chemical ordering and (ii) larger NPs with core−shell arrangements in which the core is intermixed and the outer shell is enriched in the majority element.

The inversion of core−shell chemical ordering depending on vapor composition was previously observed in laser-vaporization growth of Au−Ag NPs of 2−3 nm sizes by Liao et al.,[9] who proposed the following explanation: since bimetallic Au−Ag small clusters are energetically more favorable than their elemental counterparts, they will be predominant in the first stage of vapor condensation; these clusters will then aggregate to form the seeds of the NPs growth, i.e., the experimentally observed alloyed cores. The higher stability of binary small clusters was proved by DFT calculations on Au−Ag dimers, trimers, and tetramers. After the formation of the seeds, the metallic vapor is depleted of the minority element; in the final stage of the growth, the remaining vapor condenses forming a shell enriched in the majority element around the intermixed cores.

By means of computer simulations, we verify whether this explanation can be applied to our Pt−Pd growth, where considerably larger NPs than the Au−Ag ones are grown.[9] To this end, we first perform global optimization searches for Pt−Pd NPs of different sizes and compositions to compare equilibrium chemical ordering to the experimentally observed core−shell arrangements; we will show that the latter are clearly out-of-equilibrium, originating from kinetic-trapping effects. Then, we calculate the mixing energy of small Pt−Pd NPs with different compositions to show that mixed alloys with ∼50%−50% composition are the most energetically favorable and thus the most likely to be formed in the early growth stages. Finally, we perform growth simulations starting from a mixed Pt−Pd seed and depositing either Pt or Pd atoms to simulate the final growth stage in Pt-rich and Pd-rich atmospheres and to show that (PtPd)@Pt and (PtPd)@Pd out-of-equilibrium core−shell arrangements can be obtained, respectively.

3.2.1. Equilibrium Structures of Pt−Pd Nanoparticles. We consider Pt−Pd NPs made of 201, 586, 1289, 2406, and 4033 atoms in total, corresponding to sizes from 1.7 to 5.2 nm, which are in the range of interest of our experiments. For 201 and 586 atoms we check various compositions increasing the Pt fraction from 0.1 to 0.9 in steps of 0.1, whereas for larger sizes we consider only compositions $Pt_{0.2}Pd_{0.8}$ and $Pt_{0.8}Pd_{0.2}$. As already mentioned, all experimentally observed Pt−Pd NPs exhibit fcc geometric structures; therefore, here we consider the fcc truncated octahedral (TO) shape. The geometric shape is kept unchanged during the simulations while the chemical ordering is optimized by exchange moves between Pt and Pd atoms.[63]

The lowest-energy chemical arrangements for TO_{201} and TO_{586} NPs are shown in Figure 7. At both sizes we find clear tendencies for Pd surface segregation and Pt subsurface segregation. However, these tendencies are not extreme, since for certain compositions the core of the NP contains some Pd atoms even if the surface is not completely made of Pd (see the structures at 0.4, 0.5, and 0.6 Pt fraction in both Figures 7a and 7b), and in certain cases the core contains some Pt atoms even

https://dx.doi.org/10.1021/acs.jpcc.0c02621
J. Phys. Chem. C XXXX, XXX, XXX−XXX

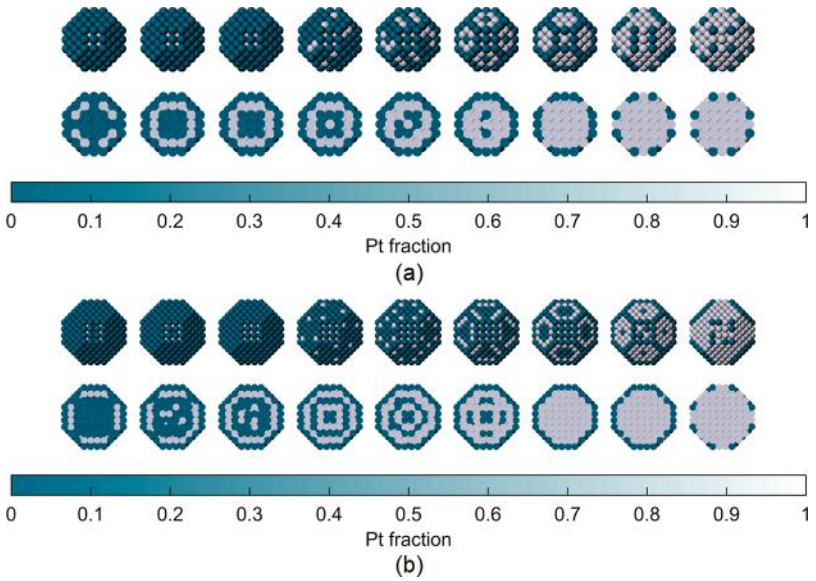

Figure 7. Equilibrium structures for (a) TO_{201} and (b) TO_{586} NPs at various compositions. The composition is expressed as Pt fraction. For each composition, the image in the top row shows the cluster surface, and the image in the bottom row shows a cross section. Here and in the following figures Pt and Pd atoms are colored in white and blue, respectively.

if the subsurface is not completely made of Pt (see the structure at 0.2 Pt fraction in Figure 7b).

At some compositions we can also observe ordered multishell arrangements. The lowest-energy chemical arrangements obtained for TO_{1289}, TO_{2496}, and TO_{4033} are shown in Figures 8 and 9 for compositions $Pt_{0.2}Pd_{0.8}$ and $Pt_{0.8}Pd_{0.2}$,

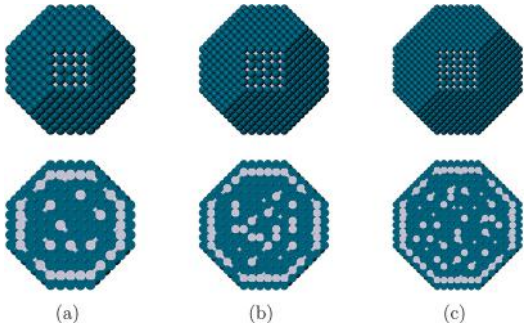

Figure 8. Equilibrium structures for (a) TO_{1289}, (b) TO_{2406}, and (c) TO_{4033} at $Pt_{0.2}Pd_{0.8}$ compositions. For each size, the image in the top row shows the cluster surface, and the image in the bottom row shows a cross section.

respectively. For all sizes, in the Pd-rich case the surface is completely made of Pd, the subsurface is enriched in Pt, and the core is almost randomly intermixed, whereas in the Pt-rich case all Pd atoms are at the surface of the NP. These results are in agreement with those by De Clercq et al.,[67] who performed Monte Carlo simulations for Pt−Pd fcc clusters up to 1289 atoms and pointed out the Pd surface and Pt subsurface segregation, as well as the formation of ordered multishell structures at small sizes.

Let us now discuss whether the experimentally observed NPs are at equilibrium or not. To this end, we point out that in none of the structures in Figures 7, 8, and 9 is the minority element concentrated in the NP core. This is evident in the Pt-rich case, in which Pd atoms are on the surface of the NP (see Figure 9), but it is true also in the Pd-rich case, in which a large

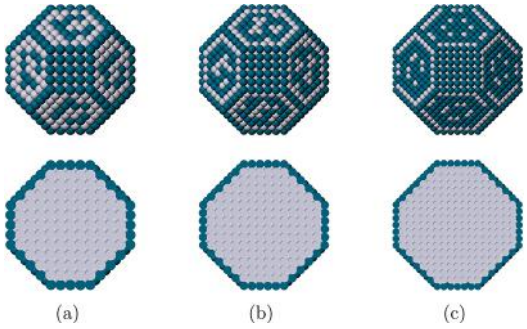

Figure 9. Equilibrium structures for (a) TO_{1289}, (b) TO_{2406}, and (c) TO_{4033} at $Pt_{0.8}Pd_{0.2}$ compositions. For each size, the image in the top row shows the cluster surface, and the image in the bottom row shows a cross section.

fraction of the Pt atoms is in the subsurface layer (see Figure 8). This allows us to establish that the experimentally observed core−shell arrangements are out-of-equilibrium configurations. On the other hand, the experimental sub-2 nm NPs, which exhibit intermixed chemical ordering, are likely to be at the equilibrium.

3.2.2. Mixing Energy. We perform mixing energy calculations for small Pt−Pd clusters of size of 50 atoms and varying composition. For each composition, we perform global optimization simulations in order to find the best isomer, and we use its energy to evaluate the mixing energy, defined as[4]

$$E_{\mathrm{mix}(\mathrm{Pt}_m\mathrm{Pd}_n)} = E_{\mathrm{b}(\mathrm{Pt}_m\mathrm{Pd}_n)} - \frac{m}{N}E_{\mathrm{b}(\mathrm{Pt}_N)} - \frac{n}{N}E_{\mathrm{b}(\mathrm{Pd}_N)} \quad (5)$$

where E_b is the binding energy and $N = m + n$ is the total number of atoms.

The mixing energy allows us to understand whether the formation of bimetallic or monometallic clusters is more favorable during the early stage of NPs growth. In particular, if $E_{\mathrm{mix}(\mathrm{Pt}_m\mathrm{Pd}_n)} < 0$, the formation of a collection of N Pt_mPd_n bimetallic clusters is energetically more favorable than the

https://dx.doi.org/10.1021/acs.jpcc.0c02621
J. Phys. Chem. C XXXX, XXX, XXX−XXX

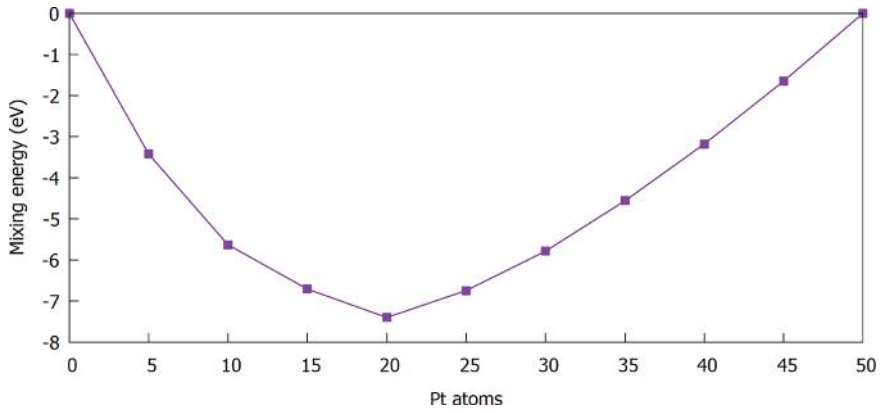

Figure 10. Mixing energy calculated for a small 50-atom Pt−Pd cluster.

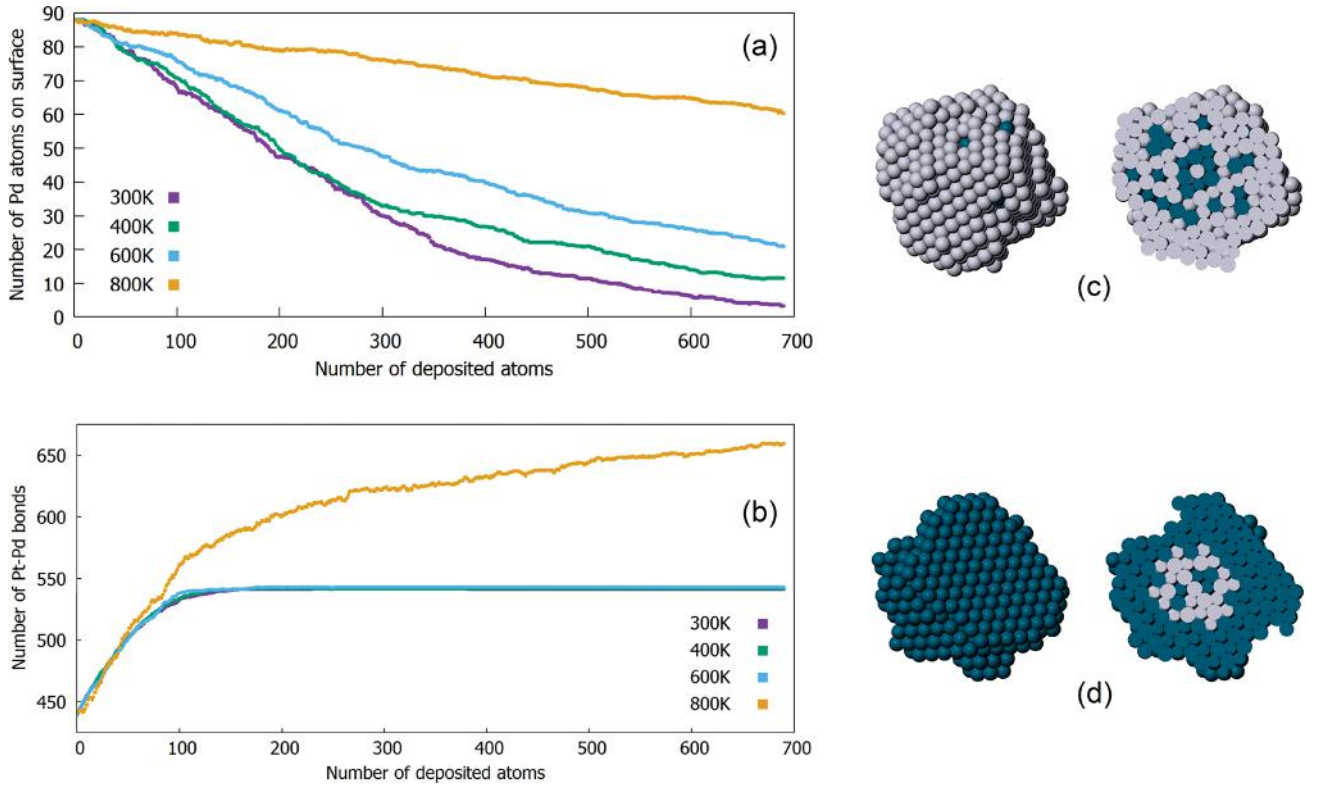

Figure 11. Graphs obtained for (a) Pt and (b) Pd deposition. For each temperature we show the average over all the five performed simulations. Core−shell structures with the outer shell enriched in (c) Pt and (d) Pd. These structures have been obtained at the end of two growth simulations at 300 K with deposition of Pt and Pd, respectively. For each structure, the image on the left shows the cluster surface, and the image on the right shows a cross section.

formation of a collection of m Pt_N + n Pd_N monometallic clusters. Vice versa, if $E_{mix(Pt_mPd_n)} > 0$, monometallic clusters are energetically more favorable. The behavior of E_{mix} is shown in Figure 10, which is negative for all compositions, with a minimum for $Pt_{20}Pd_{30}$. Therefore, the mixing of Pt and Pd atoms is energetically favorable, and thus we expect that, in the early stages of the NPs growth, bimetallic clusters will appear more frequently than monometallic ones. Among them, clusters with composition in a range close to 50%−50%, i.e., compositions close to the minimum of the mixing energy, will be the most abundant. Mixing energy calculations for smaller Pt−Pd clusters were performed previously,[68] obtaining the same type of results.

3.2.3. Nonequilibrium Chemical Ordering in Growth Simulations. In order to study the final stage of the NPs formation, we perform growth MD simulations starting from a mixed Pt−Pd seed. The seed of our simulations is the lowest-energy structure for Pt−Pd TO_{201} at 50%−50% composition (see Figure 7a). The size of the seed has been chosen because it is representative of the experimentally observed sub-2 nm population and, in some cases, of the cores of the NPs of the largest population, while the composition is close to the minimum value for the mixing energy. We consider the lowest-energy configuration since we assume that, because of its small size and because of the high temperatures in the early stage of the gas-phase growth, the seed is able to fully equilibrate. In the first set of simulations, Pt atoms are deposited on the

https://dx.doi.org/10.1021/acs.jpcc.0c02621
J. Phys. Chem. C XXXX, XXX, XXX−XXX

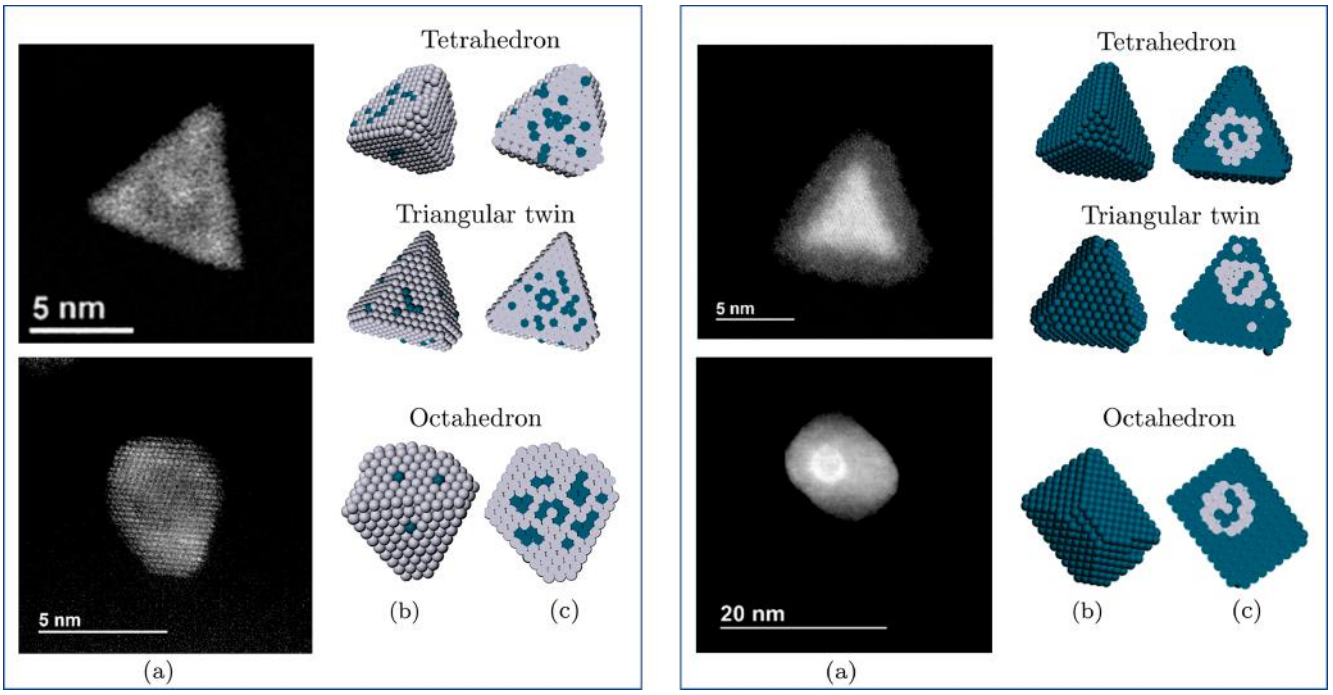

Figure 12. Comparison between typical structures of (PtPd)@Pt (left frame) and (PtPd)@Pd (right frame) NPs grown experimentally (a) and by theoretical simulations (b–c): tetrahedra/triangular twins and octahedra. For both: (a) HAADF-STEM image of the observed NPs; (b) cluster surface and (c) cross section of the corresponding structure obtained in growth simulations with deposition of Pt atoms and Pd atoms, respectively. The sizes of simulated NPs are in the range 3.5–4 nm.

starting seed. The deposition rate is 1 atom every 10 ns, and a total number of 690 atoms are deposited, up to the size of ~900 atoms. The simulations are performed at constant temperature at 300, 400, 600, and 800 K. We perform five simulations per temperature. An identical set of simulations, but with the deposition of Pd atoms, is then performed.

The aim of the simulations is to verify whether it is possible to obtain a stable outer shell made of either Pt or Pd surrounding the mixed Pt–Pd seed. Actually, we have shown that both types of core–shell arrangements are out-of-equilibrium. In the Pt-rich case, at the equilibrium, all Pd atoms are on the surface of the NP (see Figure 9); thus, the formation of a Pt outer shell may be prevented by the tendency of Pd atoms to segregate to the surface. To evaluate this effect, we monitor the number of Pd atoms on the surface of the NP during the simulations. The results are shown in Figure 11a: the evolution of the number of Pd atoms on the surface is shown for each considered temperature, as a function of the number of deposited Pt atoms. For each temperature we show the average over all the simulations. At 300, 400, and 600 K we can see a significant decrease of the number of Pd atoms on the surface. The simulations end with 3, 12, and 21 Pd surface atoms on average, respectively. We can state that, at these temperatures, the deposited Pt atoms succeed in covering the Pd atoms of the starting seed, and a stable Pt shell can actually be obtained. At 800 K we do not see a similarly significant decrease: at the end of the simulations there are on average 60 Pd atoms on the surface, which means that the majority of Pd atoms of the initial seed are able to "float" on the deposited Pt atoms and to stay on the surface.

Let us now analyze the Pd deposition case. We have shown that in Pd-rich equilibrium structures Pt atoms are randomly mixed in the interior part of the NP and enrich the subsurface layer (see Figure 8). Therefore, in this case the formation of a Pd thick outer shell may be prevented by the tendency of Pt atoms to distribute throughout the volume of the cluster, and especially below the surface. To evaluate this effect, we monitor the number of bimetallic Pt–Pd bonds. The results obtained for the four considered temperatures are shown in Figure 11b. The 300, 400, and 600 K cases exhibit the same behavior: in the first part of the simulations the number of bimetallic bonds increases since the deposited Pd atoms come into contact with the Pt atoms on the surface of the starting seed; after the first Pd layer is completed, the number of Pt–Pd bonds remains constant until the end of the simulations, meaning that Pt atoms do not mix any further. Therefore, at these temperatures, Pd atoms cover the starting seed layer by layer, and a thick pure Pd shell is formed. On the other hand, at 800 K the number of bimetallic bonds increases for the whole duration of the simulations, meaning that the Pt atoms of the seed mix with the deposited Pd atoms. At this temperature, we can still identify a Pt-enriched core (generally off-centered), but many Pt atoms are dissolved in the Pd-growing shell.

In summary, the results of the growth simulations show that core–shell arrangements with mixed core and outer shell enriched in either Pt or Pd can be obtained by depositing Pt or Pd atoms, respectively, on a mixed Pt–Pd seed. In Figures 11c and 11d we can see core–shell structures of the two types, obtained at 300 K.

The purity of the outer shell depends on the growth temperature. At higher temperatures, the tendency toward the formation of equilibrium structures (see Section 3.2) is stronger, and therefore the purity of the shell is lower. However, we can state that in both cases there is a wide range of temperatures, from 300 K to a transition temperature between 600 and 800 K, in which the core–shell arrangement is actually obtained. This result is in agreement with the

https://dx.doi.org/10.1021/acs.jpcc.0c02621
J. Phys. Chem. C XXXX, XXX, XXX–XXX

growth model described previously. In particular, it demonstrates that the formation of the seed and of the shell must occur at different times: the seed is formed in the early stage of the growth, which is known to take place at high temperatures, whereas the outer shell must form at a later stage, when the temperature of the metallic vapor has decreased; otherwise, the NP would equilibrate and the shell would not be stable enough to be observed experimentally.

3.2.4. Growth Shapes: Experiment and Simulation. Let us now analyze briefly the geometric structures of the NPs obtained at the end of the growth simulations. The greatest part of NPs presents fcc structures, with the exception of a few decahedra grown at 800 K. The overall geometry is mostly quasi-spherical at low temperatures (300 K, see Figures 11c and 11d), with a rather rough surface. At higher temperatures, a variety of quite regular geometric shapes is produced. Octahedral structures with different degrees of truncation, and sometimes with rectangular basis, are often grown. The production of these structures is indeed naturally expected in the growth from truncated octahedra since they were already observed in previous MD simulations.[65] However, also other less common growth shapes are obtained in simulations, such as truncated tetrahedral structures and flat triangular structures, which we denote as *triangular twins* since they are made of two truncated tetrahedra connected by a twin plane. Triangular twins have been recently observed in the liquid-phase growth of Ag−Au NPs.[12]

All these structures are indeed present in our experimentally grown samples. In Figure 12 we show the comparison between the STEM images of triangular and octahedral NPs and the structures obtained in the simulations for both Pt-rich and Pd-rich cases. The NPs obtained in the growth simulations show a striking resemblance with the corresponding experimental STEM images. The agreement between the geometric structures of the observed NPs and the simulated ones is a further evidence in favor of the reliability of the model used in our simulations.

4. CONCLUSIONS

In this article we provide a clear demonstration of the possibility of growing highly pure Pt−Pd NPs, which exhibit a tunable core−shell chemical ordering, in the gas phase by the magnetron-sputtering method. By means of a straightforward control of the powers applied to the Pt and Pd targets, both (PtPd)@Pt and (PtPd)@Pd NPs can be grown starting from an original atomic vapor which is either Pt-rich or Pd-rich, respectively. These NPs present an intermixed core containing both metals in similar proportions and a shell which is strongly enriched in the majority element. This result is especially remarkable for the (PtPd)@Pt case since the growth of this type of NPs previously needed a two-step procedure with postdeposition of Pt, which was anyway leading to the formation of incomplete outer shells.[30]

To provide a robust theoretical explanation of our experimental observations, we performed global optimization searches in conditions which are the closest possible to the experimental ones in terms of particle size (1.7−5.8 nm), atomic structures (truncated octahedra), and chemical composition of the original atomic vapor (this is varied from $Pt_{0.8}Pd_{0.2}$ up to $Pt_{0.2}Pd_{0.8}$). These searches showed that neither the (PtPd)@Pt nor the (PtPd)@Pd chemical ordering corresponds to thermodynamic equilibrium configurations, indicating that these structures are due to kinetic trapping effects. This is corroborated by the growth simulations which show that the growth of Pd or Pt shells on initially intermixed seeds leads to the same types of core−shell chemical ordering as obtained in the experiments.

The excellent agreement between experiments and growth simulations is not limited to the chemical ordering but very nicely extends to the geometric structures. In fact, different NP shapes are observed in the experimental samples, such as quasi-spherical and (truncated) octahedral structures, together with a few NPs of triangular symmetry. These structural types are also frequently produced in our growth simulations. These results further support the validity of our combined experiment−simulation strategy to unravel the physical origin and features of the Pt−Pd nanosystem.

In summary, our results show that the gas-phase method allows a straightforward way to control the chemical ordering of Pt−Pd NPs by which different types of long-lived metastable structures of several nanometers can be produced and observed. The physical origin underlying the production of such structures is explained in terms of mechanisms of general character, which are thus expected to be effective for a wide spectrum of materials.

■ ASSOCIATED CONTENT

Supporting Information

The Supporting Information is available free of charge at https://pubs.acs.org/doi/10.1021/acs.jpcc.0c02621.

Size distribution of Pt−Pd NPs; diffraction patterns of representative (PtPd)@Pt and (PtPd)@Pd NPs (PDF)

■ AUTHOR INFORMATION

Corresponding Authors

Riccardo Ferrando − *Dipartimento di Fisica dell'Università di Genova, Genova 16146, Italy; CNR-IMEM, Genova 16146, Italy;* orcid.org/0000-0003-2750-9061; Email: ferrando@fisica.unige.it

Chloé Minnai − *Nanoparticles by Design Unit, Okinawa Institute of Science and Technology Graduate University, Kunigami-gun, Okinawa, Japan 904-0495;* orcid.org/0000-0001-9071-5058; Email: chloe.minnai@oist.jp

Authors

Diana Nelli − *Dipartimento di Fisica dell'Università di Genova, Genova 16146, Italy*

Anjana Krishnadas − *Okinawa Institute of Science and Technology Graduate University, Kunigami-gun, Okinawa, Japan 904-0495*

Complete contact information is available at: https://pubs.acs.org/10.1021/acs.jpcc.0c02621

Author Contributions

D.N. performed the global optimization searches. D.N. and R.F. performed and analyzed the growth simulations. C.M. conceived and performed the experiments, TEM characterizations, and analysis. A.K. supported with data analysis. D.N., R.F., and C.M. wrote the manuscript. All authors have given approval to the final version of the manuscript.

Notes

The authors declare no competing financial interest.

https://dx.doi.org/10.1021/acs.jpcc.0c02621
J. Phys. Chem. C XXXX, XXX, XXX−XXX

■ ACKNOWLEDGMENTS

The research performed at OIST was supported by funding from the Okinawa Institute of Science and Technology Graduate University. C.M. is also grateful to Prof. Andrea Falqui for insightful discussions and to Toshio Sasaki for assistance. The authors thank Ella Joyce Minnai for technical drawing. The authors acknowledge networking support from the International Research Network Nanoalloys of CNRS.

■ REFERENCES

(1) Ferrando, R.; Jellinek, J.; Johnston, R. L. Nanoalloys: From Theory to Applications of Alloy Clusters and Nanoparticles. *Chem. Rev. (Washington, DC, U. S.)* **2008**, *108*, 845−910.
(2) Ghosh Chaudhuri, R.; Paria, S. Core/Shell Nanoparticles: Classes, Properties, Synthesis Mechanisms, Characterization, and Applications. *Chem. Rev.* **2012**, *112*, 2373−2433 PMID: 22204603..
(3) Calvo, F., Ed. *Nanoalloys from Fundamentals to Emergent Applications*; Elsevier: Amsterdam, Netherlands, 2013.
(4) Ferrando, R. *Structure and Properties of Nanoalloys*; Frontiers of Nanoscience, Vol. 10; Elsevier: Amsterdam, Netherlands, 2016.
(5) Gilroy, K. D.; Ruditskiy, A.; Peng, H.-C.; Qin, D.; Xia, Y. Bimetallic Nanocrystals: Syntheses, Properties, and Applications. *Chem. Rev.* **2016**, *116*, 10414−10472.
(6) Llamosa, D.; Ruano, M.; Martinez, L.; Mayoral, A.; Roman, E.; Garcia-Hernández, M.; Huttel, Y. The ultimate step towards a tailored engineering of core@ shell and core@ shell@ shell nanoparticles. *Nanoscale* **2014**, *6*, 13483−13486.
(7) Wells, D. M.; Rossi, G.; Ferrando, R.; Palmer, R. E. Metastability of the atomic structures of size-selected gold nanoparticles. *Nanoscale* **2015**, *7*, 6498−6504.
(8) Grammatikopoulos, P.; Kioseoglou, J.; Galea, A.; Vernieres, J.; Benelmekki, M.; Diaz, R. E.; Sowwan, M. Kinetic trapping through coalescence and the formation of patterned Ag-Cu nanoparticles. *Nanoscale* **2016**, *8*, 9780−9790.
(9) Liao, T.-W.; Yadav, A.; Hu, K.-J.; van der Tol, J.; Cosentino, S.; D'Acapito, F.; Palmer, R. E.; Lenardi, C.; Ferrando, R.; Grandjean, D.; et al. Unravelling the nucleation mechanism of bimetallic nanoparticles with composition-tunable core-shell arrangement. *Nanoscale* **2018**, *10*, 6684−6694.
(10) Pirart, J.; Front, A.; Rapetti, D.; Andreazza-Vignolle, C.; Andreazza, P.; Mottet, C.; Ferrando, R. Reversed size-dependent stabilization of ordered nanophases. *Nat. Commun.* **2019**, *10*, 1982.
(11) Vernieres, J.; Steinhauer, S.; Zhao, J.; Grammatikopoulos, P.; Ferrando, R.; Nordlund, K.; Djurabekova, F.; Sowwan, M. Site-Specific Wetting of Iron Nanocubes by Gold Atoms in Gas-Phase Synthesis. *Advanced Science* **2019**, *6*, 1900447.
(12) Ahmad, N.; Bon, M.; Passerone, D.; Erni, R. Template-Assisted in Situ Synthesis of Ag@Au Bimetallic Nanostructures Employing Liquid-Phase Transmission Electron Microscopy. *ACS Nano* **2019**, *13*, 13333−13342.
(13) Nelli, D.; Ferrando, R. Core-shell vs. multi-shell formation in nanoalloy evolution from disordered configurations. *Nanoscale* **2019**, *11*, 13040−13050.
(14) Bochicchio, D.; Ferrando, R. Morphological instability of core-shell metallic nanoparticles. *Phys. Rev. B: Condens. Matter Mater. Phys.* **2013**, *87*, 165435.
(15) Ferrando, R. Symmetry breaking and morphological instabilities in core-shell metallic nanoparticles. *J. Phys.: Condens. Matter* **2015**, *27*, 013003.
(16) Esparza, R.; Garcia-Ruiz, A. F.; Salazar, J. J. V.; Pérez, R.; José-Yacamán, M. Structural characterization of Pt−Pd core−shell nanoparticles by Cs-corrected STEM. *J. Nanopart. Res.* **2013**, *15*, 1342.
(17) Martinez, L.; Mayoral, A.; Espiñeira, M.; Roman, E.; Palomares, F. J.; Huttel, Y. Core@ shell, Au@ TiO x nanoparticles by gas phase synthesis. *Nanoscale* **2017**, *9*, 6463−6470.
(18) Anandan, S.; Grieser, F.; Ashokkumar, M. Sonochemical Synthesis of Au-Ag Core-Shell Bimetallic Nanoparticles. *J. Phys. Chem. C* **2008**, *112*, 15102−15105.
(19) Zhang, H.; Jin, M.; Xia, Y. Enhancing the catalytic and electrocatalytic properties of Pt-based catalysts by forming bimetallic nanocrystals with Pd. *Chem. Soc. Rev.* **2012**, *41*, 8035−8049.
(20) Lim, B.; Jiang, M.; Camargo, P. H. C.; Cho, E. C.; Tao, J.; Lu, X.; Zhu, Y.; Xia, Y. Pd-Pt Bimetallic Nanodendrites with High Activity for Oxygen Reduction. *Science* **2009**, *324*, 1302−1305.
(21) Peng, Z.; Yang, H. Synthesis and Oxygen Reduction Electrocatalytic Property of Pt-on-Pd Bimetallic Heteronanostructures. *J. Am. Chem. Soc.* **2009**, *131*, 7542−7543.
(22) Wang, L.; Nemoto, Y.; Yamauchi, Y. Direct Synthesis of Spatially-Controlled Pt-on-Pd Bimetallic Nanodendrites with Superior Electrocatalytic Activity. *J. Am. Chem. Soc.* **2011**, *133*, 9674−9677.
(23) Yin, A.-X.; Min, X.-Q.; Zhang, Y.-W.; Yan, C.-H. Shape-Selective Synthesis and Facet-Dependent Enhanced Electrocatalytic Activity and Durability of Monodisperse Sub-10 nm Pt-Pd Tetrahedrons and Cubes. *J. Am. Chem. Soc.* **2011**, *133*, 3816−3819.
(24) Huang, R.; Wen, Y.-H.; Zhu, Z.-Z.; Sun, S.-G. Pt−Pd bimetallic catalysts: structural and thermal stabilities of core−shell and alloyed nanoparticles. *J. Phys. Chem. C* **2012**, *116*, 8664−8671.
(25) Long, N. V.; Hien, T. D.; Asaka, T.; Ohtaki, M.; Nogami, M. Synthesis and characterization of Pt−Pd alloy and core-shell bimetallic nanoparticles for direct methanol fuel cells (DMFCs): Enhanced electrocatalytic properties of well-shaped core-shell morphologies and nanostructures. *Int. J. Hydrogen Energy* **2011**, *36*, 8478−8491.
(26) Mougenot, M.; Caillard, A.; Brault, P.; Baranton, S.; Coutanceau, C. High Performance plasma sputtered PdPt fuel cell electrodes with ultra low loading. *Int. J. Hydrogen Energy* **2011**, *36*, 8429−8434.
(27) Yoo, S. J.; Park, H. Y.; Jeon, T. Y.; Park, I. S.; Cho, Y. H.; Sung, Y. E. Promotional effect of palladium on the hydrogen oxidation reaction at a PtPd alloy electrode. *Angew. Chem., Int. Ed.* **2008**, *47*, 9307−9310.
(28) Lee, H.; Habas, S. E.; Somorjai, G. A.; Yang, P. Localized Pd overgrowth on cubic Pt nanocrystals for enhanced electrocatalytic oxidation of formic acid. *J. Am. Chem. Soc.* **2008**, *130*, 5406−5407.
(29) Huang, D.-B.; Yuan, Q.; Wang, H.-H.; Zhou, Z.-Y. Facile synthesis of PdPt nanoalloys with sub-2.0 nm islands as robust electrocatalysts for methanol oxidation. *Chem. Commun.* **2014**, *50*, 13551−13554.
(30) Caillard, A.; Cuynet, S.; Lecas, T.; Andreazza, P.; Mikikian, M.; Thomann, A.-L.; Brault, P. PdPt catalyst synthesized using a gas aggregation source and magnetron sputtering for fuel cell electrodes. *J. Phys. D: Appl. Phys.* **2015**, *48*, 475302.
(31) Rapallo, A.; Rossi, G.; Ferrando, R.; Fortunelli, A.; Curley, B. C.; Lloyd, L. D.; Tarbuck, G. M.; Johnston, R. L. Global optimization of bimetallic cluster structures. I. Size-mismatched Ag-Cu, Ag-Ni, and Au-Cu systems. *J. Chem. Phys.* **2005**, *122*, 194308.
(32) Paz-Borbón, L. O.; Johnston, R. L.; Barcaro, G.; Fortunelli, A. A Mixed Structural Motif in 34-Atom Pd-Pt Clusters. *J. Phys. Chem. C* **2007**, *111*, 2936−2941.
(33) Yuan, Q.; Zhou, Z.; Zhuang, J.; Wang, X. Pd−Pt random alloy nanocubes with tunable compositions and their enhanced electrocatalytic activities. *Chem. Commun.* **2010**, *46*, 1491−1493.
(34) Habas, S. E.; Lee, H.; Radmilovic, V.; Somorjai, G. A.; Yang, P. Shaping binary metal nanocrystals through epitaxial seeded growth. *Nat. Mater.* **2007**, *6*, 692−697.
(35) Wang, Y.; Toshima, N. Preparation of Pd- Pt bimetallic colloids with controllable core/shell structures. *J. Phys. Chem. B* **1997**, *101*, 5301−5306.
(36) Bonet, F.; Delmas, V.; Grugeon, S.; Urbina, R. H.; Silvert, P.-Y.; Tekaia-Elhsissen, K. Sythesis of Monodisperse Au, Pt, Pd, Ru and Ir Nanoparticles in Ethylene Glycol. *Nanostruct. Mater.* **1999**, *11*, 1277−1284.
(37) Martinez, L.; Diaz, M.; Roman, E.; Ruano, M.; Llamosa Perez, D.; Huttel, Y. Generation of nanoparticles with adjustable size and

https://dx.doi.org/10.1021/acs.jpcc.0c02621
J. Phys. Chem. C XXXX, XXX, XXX−XXX

controlled stoichiometry: recent advances. *Langmuir* **2012**, *28*, 11241−11249.
(38) Russo, R.; Cianchi, A.; Akhmadeev, Y. H.; Catani, L.; Langner, J.; Lorkiewicz, J.; Polini, R.; Ruggiero, B.; Sadowski, M. J.; Tazzari, S.; et al. UHV arc for high quality film deposition. *Surf. Coat. Technol.* **2006**, *201*, 3987−3992.
(39) Huttel, Y. *Gas-Phase Synthesis of Nanoparticles*; John Wiley & Sons: New York, 2017.
(40) Haberland, H., Ed. *Clusters of Atoms and Molecules*; Springer: Berlin, Germany, 1994.
(41) Huttel, Y.; Martinez, L.; Mayoral, A.; Fernández, I. Gas-phase synthesis of nanoparticles: present status and perspectives. *MRS Commun.* **2018**, *8*, 947−954.
(42) Nakaya, M.; Iwasa, T.; Tsunoyama, H.; Eguchi, T.; Nakajima, A. Formation of a superatom monolayer using gas-phase-synthesized Ta@ Si 16 nanocluster ions. *Nanoscale* **2014**, *6*, 14702−14707.
(43) Plant, S. R.; Cao, L.; Palmer, R. E. Atomic structure control of size-selected gold nanoclusters during formation. *J. Am. Chem. Soc.* **2014**, *136*, 7559−7562.
(44) Johnson, G. E.; Colby, R.; Laskin, J. Soft landing of bare nanoparticles with controlled size, composition, and morphology. *Nanoscale* **2015**, *7*, 3491−3503.
(45) Mayoral, A.; Llamosa, D.; Huttel, Y. A novel Co@ Au structure formed in bimetallic core@ shell nanoparticles. *Chem. Commun.* **2015**, *51*, 8442−8445.
(46) Faraone, G.; Modi, R.; Marom, S.; Podestà, A.; Di Vece, M. Increasing the optical absorption in a-Si thin films by embedding gold nanoparticles. *Opt. Mater.* **2018**, *75*, 204−210.
(47) Mirigliano, M.; Borghi, F.; Antidormi, A.; Colombo, L.; Milani, P.; Podesta, A. Non-ohmic behavior and resistive switching of Au cluster-assembled films beyond the percolation threshold. *Nanoscale Advances* **2019**, *1*, 3119.
(48) Minnai, C.; Cremonesi, L.; Milani, P.; Potenza, M. A. A very simple scheme for spectrally resolved imaging by means of curved polymeric gratings. *Mater. Res. Express* **2019**, *6*, 065044.
(49) Shirai, S.; Acharya, S. K.; Bose, S. K.; Mallinson, J. B.; Galli, E.; Pike, M. D.; Arnold, M. D.; Brown, S. A. Long-range temporal correlations in scale-free neuromorphic networks. *Network Neuroscience* **2020**, *4*, 432.
(50) Vahl, A.; Carstens, N.; Strunskus, T.; Faupel, F.; Hassanien, A. Diffusive Memristive Switching on the Nanoscale, from Individual Nanoparticles towards Scalable Nanocomposite Devices. *Sci. Rep.* **2019**, *9*, 1−10.
(51) Hirata, N.; Sato, M.; Tsunemi, E.; Watanabe, Y.; Tsunoyama, H.; Nakaya, M.; Eguchi, T.; Negishi, Y.; Nakajima, A. Fabrication and Characterization of Floating Memory Devices Based on Thiolate-Protected Gold Nanoclusters. *J. Phys. Chem. C* **2017**, *121*, 10638−10644.
(52) Minnai, C.; Mirigliano, M.; Brown, S. A.; Milani, P. The nanocoherer: an electrically and mechanically resettable resistive switching device based on gold clusters assembled on paper. *Nano Futures* **2018**, *2*, 11002.
(53) Mallinson, J.; Shirai, S.; Acharya, S.; Bose, S.; Galli, E.; Brown, S. Avalanches and criticality in self-organized nanoscale networks. *Science advances* **2019**, *5*, No. eaaw8438.
(54) Minnai, C.; Di Vece, M.; Milani, P. Mechanical-optical-electro modulation by stretching a polymer-metal nanocomposite. *Nanotechnology* **2017**, *28*, 355702.
(55) Bai, Z.; Liu, X.; Lian, Z.; Zhang, K.; Wang, G.; Shi, S.-F.; Pi, X.; Song, F. A Silicon Cluster Based Single Electron Transistor with Potential Room-Temperature Switching. *Chin. Phys. Lett.* **2018**, *35*, 037301.
(56) Minnai, C.; Bellacicca, A.; Brown, S. A.; Milani, P. Facile fabrication of complex networks of memristive devices. *Sci. Rep.* **2017**, *7*, 1−8.
(57) Du Plessis, J.; Van Wyk, G. N.; Taglauer, E. Preferential sputtering and radiation enhanced segregation in palladium-platinum alloys. *Surf. Sci.* **1989**, *220*, 381−390.
(58) Mayoral, A.; Mejia-Rosales, S.; Mariscal, M. M.; Perez-Tijerina, E.; Jose-Yacaman, M. The Co-Au interface in bimetallic nanoparticles: a high resolution STEM study. *Nanoscale* **2010**, *2*, 2647−2651.
(59) Baker, S.; Thornton, S.; Keen, A.; Preston, T.; Norris, C.; Edmonds, K.; Binns, C. The construction of a gas aggregation source for the preparation of mass-selected ultrasmall metal particles. *Rev. Sci. Instrum.* **1997**, *68*, 1853−1857.
(60) Khojasteh, M.; Kresin, V. V. Influence of source parameters on the growth of metal nanoparticles by sputter-gas-aggregation. *Appl. Nanosci.* **2017**, *7*, 875−883.
(61) Cyrot-Lackmann, F.; Ducastelle, F. Binding Energies of Transition-Metal Atoms Adsorbed on a Transition Metal. *Phys. Rev. B* **1971**, *4*, 2406−2412.
(62) Rosato, V.; Guillopé, M.; Legrand, B. Thermodynamical and structural properties of f.c.c. transition metals using a simple tight-binding model. *Philos. Mag. A* **1989**, *59*, 321.
(63) Rossi, G.; Ferrando, R. Searching for low-energy structures of nanoparticles: a comparison of different methods and algorithms. *J. Phys.: Condens. Matter* **2009**, *21*, 084208.
(64) Baletto, F.; Mottet, C.; Ferrando, R. Microscopic mechanisms of the growth of metastable silver icosahedra. *Phys. Rev. B: Condens. Matter Mater. Phys.* **2001**, *63*, 155408.
(65) Baletto, F.; Mottet, C.; Ferrando, R. Molecular dynamics simulations of surface diffusion and growth on silver and gold clusters. *Surf. Sci.* **2000**, *446*, 31−45.
(66) Popok, V. N.; Gurevich, L. Charge states of size-selected silver nanoparticles produced by magnetron sputtering. *J. Nanopart. Res.* **2019**, *21*, 171.
(67) De Clercq, A.; Giorgio, S.; Mottet, C. Pd surface and Pt subsurface segregation in Pt1-cPdcnanoalloys. *J. Phys.: Condens. Matter* **2016**, *28*, 064006.
(68) Paz-Borbón, L. O.; Gupta, A.; Johnston, R. L. Dependence of the structures and chemical ordering of Pd-Pt nanoalloys on potential parameters. *J. Mater. Chem.* **2008**, *18*, 4154−4164.

https://dx.doi.org/10.1021/acs.jpcc.0c02621
J. Phys. Chem. C XXXX, XXX, XXX−XXX